Supplemental Information

Zhouyin Wei[1,2,‡], Qilin Zhou[1,3,‡], Xiuxiu Niu[1,3], Shunchang Liu[1], Zijing Dong[1,3], Haoming Liang[1,3], Jinxi Chen[1,3], Zhuojie Shi[1,3,4], Xi Wang[1,3], Zhenrong Jia[1,3], Xiao Guo[1,3], Renjun Guo[1,6], Xin Meng[1,3,4], Yu-Duan Wang[1,3], Nengxu Li[1,3], Zhiguang Xu[5], Zaifang Li[5], Armin Gerhard Aberle[1,2], Xinxing Yin[5,*], Yi Hou[1,3,*]

[1]Solar Energy Research Institute of Singapore (SERIS), National University of Singapore, Singapore, 117574, Singapore
[2]Department of Electrical and Computer Engineering, National University of Singapore, Singapore, 117583, Singapore
[3]Department of Chemical and Biomolecular Engineering, National University of Singapore, Singapore, 117585, Singapore
[4]Joint School of National University of Singapore and Tianjin University, International Campus of Tianjin University Fuzhou, Fuzhou, 350207, China
[5]China-Australia Institute for Advanced Materials and Manufacturing (IAMM), Jiaxing University, Jiaxing 314001, China
[6]Present address: Institute of Microstructure Technology, Karlsruhe Institute of Technology, Eggenstein-Leopoldshafen, 76344, Germany

*Correspondence to: xxyin@zjxu.edu.cn and yi.hou@nus.edu.sg
‡These authors contributed equally

Experimental part

Materials

Dimethyl sulfoxide (DMSO, 99.8%), N, N-dimethylformamide (DMF, 99.9%), anisole (anhydrous, 99.7%), isopropanol (IPA, 99.9%), ethanol (anhydrous, 99.5%), lead chloride ($PbCl_2$), tin(II) iodide (SnI_2, anhydrobeads, 99.99% trace metals basis), tin(II) fluorine (SnF_2), and cesium iodide (CsI, 99.99%) were purchased from Sigma-Aldrich. Lead iodide (PbI_2) and lead bromide ($PbBr_2$) were purchased from Tokyo Chemical Industry. Silver was purchased from Kurt J. Lesker. C_{60} and bathocuproine (BCP) were purchased from Lumtec. Formamidinium iodide (FAI), methylammonium iodide (MAI), methylammonium chloride (MACl), and ethane-1,2-diammonium iodide (EDAI, 98%) were obtained from Greatcell solar materials. ITO substrates (X07-20AC) were purchased from Suzhou Shangyang Solar Technology Co. PEDOT: PSS aqueous solution (no. Al 4083) was purchased from Xi'an Polymer Light Technology. Tin(IV) oxide (SnO_2, 15% in H_2O) was purchased from Alfa Aesar.

Single-junction wide-bandgap perovskite solar cell fabrication

Firstly, the ITO glass was ultrasonically cleaned with detergent for 15 min and then washed with acetone and IPA, respectively, for 15 min. After UVO treatment for 15 min, the substrates were transferred to a nitrogen glove box. The three SAMs, DCB-C4POH, DCB-Br-1, and DCB-Br-2 (1 mg/ml in ethanol) were spin-coated on the substrates at 4,000 rpm for 30 s and then heated at 100 °C for 10 min. The 1.1 M WBG perovskite precursor solution $Cs_{0.2}FA_{0.8}Pb(I_{0.6}Br_{0.4})_3$ was prepared by dissolving CsI, FAI, $PbBr_2$, and PbI_2 in a mixture of solvents DMF and DMSO at a volume ratio of 4:1. The precursor solution was shaken at 60 °C overnight. After fully dissolved, 3% $PbCl_2$ and MACl were added to the precursor. Then, the WBG perovskite precursor was spin-coated on the substrate at 4,000 rpm for 45 s with an acceleration of 2,000 rpm/s and N_2 gas was blown on top of the spinning substrate after 15 s. The perovskite film was annealed at 100 °C for 10 min. Then the perovskite films were treated by an $EDAI_2$ solution dissolved in IPA with a concentration of 1 mg/ml at 3,000 rpm for 30 s, and then annealed at 100 °C for 10 min. Lastly, C_{60} (20 nm)/BCP (8 nm)/Ag (100 nm) were deposited by a high-vacuum thermal evaporator to complete the device fabrication.

Single-junction narrow-bandgap perovskite solar cell fabrication

Firstly, the ITO glass was cleaned and UVO treated as mentioned above. PEDOT: PSS was spin-coated on the substrates at 6,000 rpm for 30 s and annealed at 150 °C for 10 min. Substrates were then transferred to a nitrogen glove box for the deposition of NBG film. The 2.0 M NBG perovskite precursor solution $Cs_{0.05}FA_{0.7}MA_{0.25}Pb_{0.5}Sn_{0.5}I_3$ was prepared by dissolving CsI, MAI, FAI, SnI_2, and PbI_2 in a mixture of DMF and DMSO at a volume ratio of 3:1 and 5% SnF_2 were added. The precursor was stirred at room temperature for 1 h and then filtered using a 0.22 μm polytetrafluoroethylene membrane before use. Then the NBG perovskite precursor was spin-coated on the substrate with a two-step procedure: (1) 1,000rpm for 10 s with an acceleration of 500 rpm/s and (2) 4,000 rpm for 45 s with an acceleration of 1,000 rpm/s, 250 μl anisole was slowly dropped onto the substrates at the last 7 s before the ending. The samples were then annealed at 100 °C for 10 min. Post-treatment with 1 mg/ml EDAI in IPA was carried out by spin-coating the solution at 3,000 rpm for 30 s, followed by 10 min 100 °C annealing. Lastly, C_{60} (20 nm)/BCP (8 nm)/Ag (100 nm) were deposited by a high-vacuum thermal evaporator to complete the NBG device fabrication.

All-perovskite tandem solar cells

The WBG subcell was prepared by the method described above (before ALD SnO_X). For the tandem device, we replaced the BCP in the WBG subcell with SnO_X as the buffer layer because BCP is thermally unstable and cannot adequately protect the WBG subcell during the subsequent fabrication of the NBG subcell. After evaporating 20 nm of C_{60}, a thick 20 nm-SnO_X was deposited by an atomic layer deposition (ALD) system to create a compact and dense barrier layer against sputtering and solvent damage. Then the samples were transferred to a low-damage magnetron sputtering system to deposit a very thin layer of ITO (5 nm). The thickness of the ITO is carefully optimized to avoid shunting and mitigate the S-shaped J-V curve. After that, the samples were transferred to a plasma machine for 5 s treatment with 250 W power for ITO treatment. Next, PEDOT: PSS was diluted with IPA at a 1:2 volume ratio to minimize potential damage to the underlying ICL and WBG subcell, as the water-based solution of PEDOT: PSS can adversely affect the underlying layers. The

diluted PEDOT:PSS was spin-coated on the substrates at 5,000 rpm for 30 s and annealed at 100 °C for 10 min. Substrates were then transferred to a nitrogen glove box for the deposition of NBG subcells. The NBG perovskite film was deposited and post-treated as mentioned above. Finally, C_{60} (20 nm)/BCP (8 nm)/Ag (100 nm) were deposited to complete the tandem device fabrication. We optimized the WBG and NBG perovskite layer thicknesses by adjusting the spin-coating speeds. The optimized spin speeds are 5000 rpm for the WBG perovskite and 3500 rpm for the NBG perovskite.

Film characterization

The UV-Vis absorbance and transmittance spectra were recorded with the Agilent Cary 7000 universal measurement spectrophotometer. XRD profiles were recorded with an X-ray diffractometer (D8, Bruker) with Cu Kα radiation (λ = 0.1542 nm). The ^{1}H NMR and ^{13}C NMR spectra were conducted on a Bruker Avance 500 MHz spectrometer. Mass spectra were measured using gas chromatography-mass spectrometry (GC-MS). TRPL measurements were conducted by PicoQuant FluoTime 300 spectrometer with laser excitation at 515.8 nm in ambient air. SEM images were taken with Regulus SU8200 system (Hitachi) at 1 kV accelerating voltage under SE mode. PL measurements and PLQY were tested through LuQY Pro from QYB (Quantum yield Berlin). A continuous laser with a wavelength of 515 nm was set to provide a photon flux equivalent to 1 sun intensity. For intensity-dependent V_{OC} measurements, the intensity was varied between 0.01 and 1.3 sun and stabilized for 15 min before measurements. The plotting of p-*JV* follows previous report,[1] assuming a J_{SC} of 18.5 mA cm^{-2} (93% of S-Q current limit) to avoid potential influences. Confocal photoluminescence mappings were measured on a Nikon A1 confocal microscope equipped with a 633-nm continuous-wave laser. XPS (source: Al Kα X-ray) and UPS (source: He(I)- 21.22 eV) measurements were obtained using a Kratos AXIS Supra+ X-ray photoelectron spectrometer. AFM and KPFM measurements were conducted with the Park NX20 system. AFM measurements were conducted with non-contact mode (NCM). Frequency modulation mode (sideband KPFM) was applied throughout the measurements to obtain better contrasts and higher resolution.

Device characterizations

The device *JV* measurements were determined using a Keithley 2400 source meter under simulated 1-sun AM 1.5G illumination (100 mW cm^{-2}) provided by an ABET Technologies Sun 2000 solar simulator and Wavelabs SINUS-220. The solar simulator is calibrated by a WPVS reference cell from Fraunhofer-ISE. The *JV* curves were measured using both forward scan, ranging from -0.2 V to 1.4 V (-0.2 V to 2.15 V for tandem devices), and reverse scan, ranging from 1.2 V to 0.2 V (2.15 V to -0.2 V for tandem devices), with a scan step size of 20 mV masked by metal aperture masks with an active area of 0.055 cm^2. The integration time is 10 ms and the dwell time is 10 ms. All device tests were performed in a nitrogen glove box (20 °C) with oxygen concentration below 0.01 ppm and humidity below 0.01 ppm. The 300s MPPT measurements for tandem devices were conducted with the same setup. The dark JV curves were measured using a forward scan, ranging from -0.5 V to 1.5 V, with a scan step size of 20 mV. The SCLC curves were measured based on hole-only devices (glass/ITO/SAMs/perovskite/PTAA/MoO_x/Ag) using forward scan, ranging from 0 V to 4 V, with a scan step size of 10 mV. A Bentham PVE300-IVT system was used to obtain the EQE curve. The LED laser intensity used in the measurements was calibrated using built-in silicon and germanium diodes. For the tandem device, the light bias from a halogen lamp with a 600-nm short-pass filter and a 750-nm long-pass filter from Thorlabs were used to measure the spectral lines of the WBG and NBG subcells, respectively. For the high-resolution EQE, the light was chopped at 137 Hz and coupled into a Bentham monochromator. The resulting monochromatic light was focused onto the perovskite solar cell, and its current under short-circuit conditions was fed to a current preamplifier (Stanford SR 570) before it was analyzed with a lock-in amplifier (Stanford SR830 DSP). The time constant of the lock-in amplifier was chosen to be 1 s, and the amplification of the preamplifier was increased to resolve low photocurrents. The EQE was determined by dividing the photocurrent of the cell by the flux of incoming photons, which was measured using a calibrated Si photodiode. All EQE measurements have been performed at ambient conditions at 25 °C with relative humidity of around 60% and with the edge-sealing encapsulation using UV resin. Long-term MPP tracking of the tandem devices was measured with the MPP Tracking-4B system (Shenzhen Lancheng Technology) with LED simulated AM 1.5 G spectrum. The measurements were carried out in air at 25 °C with a relative humidity of about 85% with encapsulated devices. The cross-sectional SEM image of tandem device was taken by a Hitachi Regulus SU8200 system at 1 kV accelerating voltage under SE mode.

Simulation details

Electrostatic surface potential (ESP) simulations and HOMOs/LUMOs were calculated by Gaussian 09 program package with B3LYP/6-311G basis.

Chemical synthesis

DCB-C4POH[2], **DCB-Br-1**[3], and compund **1**[4] were synthesized as reported. For the synthesis of **DCB-Br-2**, the detailed procedures are listed below:

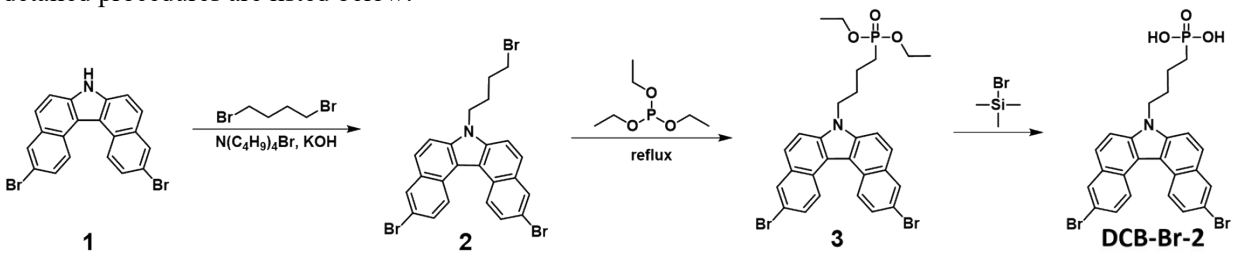

Scheme S1. Synthetic route of DCB-Br-2.

3,11-dibromo-7-(4-bromobutyl)-7H-dibenzo[c,g]carbazole (Compund **2**)

Compund **1** (5.00 g, 11.76 mmol) was dissolved in 1,4-dibromobutane (50.79 g, 235.23 mmol) and 50% KOH aqueous solution (6.60 g, 58.81 mmol). Tetrabutylammonium bromide (0.57 g, 1.76 mmol) was added at room temperature. The mixed solution was stirred at 65 ℃ overnight. The crude mixture was extracted with CH_2Cl_2, washed with water, the combined organic phase was dried over by $MgSO_4$ and concentrated in vacuo. The residue was purified by column chromatography (petroleum ether/CH_2Cl_2, 5:1, v/v) to afford compund **2** as white solid (4.75 g, 72%). ^{1}H NMR (400 MHz, $CDCl_3$, δ): 8.89 (d, J = 9.0 Hz, 2H), 8.14 (d, J = 2.1 Hz, 2H), 7.78 (d, J = 8.8 Hz, 2H), 7.71 – 7.64 (m, 4H), 4.52 (t, J = 7.2 Hz, 2H), 3.36 (t, J = 6.4 Hz, 2H), 2.14 – 2.05 (m, 2H), 1.91 (dd, J = 8.7, 6.2 Hz, 2H).

Diethyl (4-(3,11-dibromo-7H-dibenzo[c,g]carbazol-7-yl)butyl)phosphonate (Compund **3**)

Compound **2** (3.00 g, 5.36 mmol) was dissolved in triethyl phosphite (17.80 g, 107.12 mmol) and heated to reflux overnight. The extra solvent was distilled off under reduced pressure. The residue was purified by column chromatography (petroleum ether/ethyl acetate, 1:1, v/v) to afford compund **3** as colorless oil (2.77 g, 84%). ^{1}H NMR (400 MHz, $CDCl_3$, δ): 8.92 (d, J = 9.0 Hz, 2H), 8.15 (d, J = 2.1 Hz, 2H), 7.80 (d, J = 8.9 Hz, 2H), 7.70 (dd, J = 8.9, 1.7 Hz, 4H), 4.54 (t, J = 7.2 Hz, 2H), 3.99 (dqd, J = 8.4, 7.1, 1.5 Hz, 4H), 2.11 – 1.98 (m, 2H), 1.78 – 1.65 (m, 4H), 1.20 (t, J = 7.1 Hz, 6H).

(4-(3,11-Dibromo-7H-dibenzo[c,g]carbazol-7-yl)butyl)phosphonic acid (**DCB-Br-2**)

Compound **3** (2.50 g, 4.05 mmol) was dissolved in anhydrous THF (40 mL) and protected by nitrogen atmosphere. Then bromotrimethylsilane (6.20 g, 40.50 mmol) was added dropwise. The mixture was stirred at room temperature for 24 h. After that, methanol (40 mL) was added and the solution was stirred for another 3 h. Finally, the crude mixture was concentrated under vacuum and then 400 mL distilled water was added and the opaque solution was stirred for 24 h. The crude product was filtered off and washed with water. The crude product was dissolved in THF (3 ml) and precipitated into *n*-hexane (50 ml) for 3 times. **DCB-Br-2** was filtered and washed with ethyl acetate. After drying in vacuum, **DCB-Br-2** was obtained as white solid (1.65 g, 73%). ^{1}H NMR (400 MHz, DMSO-d_6, δ): 8.88 (d, J = 9.0 Hz, 2H), 8.36 (d, J = 2.2 Hz, 2H), 8.10 (d, J = 9.0 Hz, 2H), 7.99 (d, J = 8.9 Hz, 2H), 7.78 (dd, J = 9.0, 2.2 Hz, 2H), 4.69 (t, J = 7.2 Hz, 2H), 1.89 (s, 2H), 1.59 – 1.48 (m, 4H). ^{13}C NMR (100 MHz, DMSO-d_6, δ): 136.96, 130.75, 128.10, 126.76, 125.98, 125.71, 115.61, 115.53, 112.84, 42.39, 30.59, 30.44, 27.86, 26.50, 20.36, 20.31. MALDI-TOF MS: m/z=558.9548 $[M]^+$, calcd. for $C_{24}H_{20}Br_2NO_3P$: 558.9533.

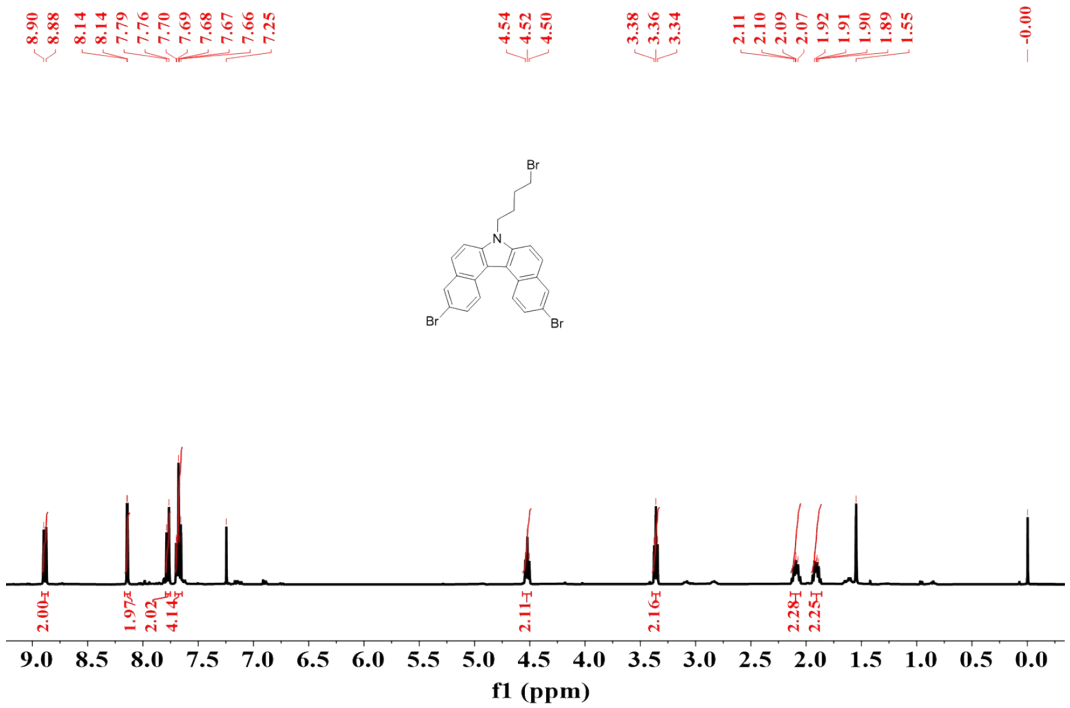

Figure S1. ^{1}H NMR spectrum for compund 2.

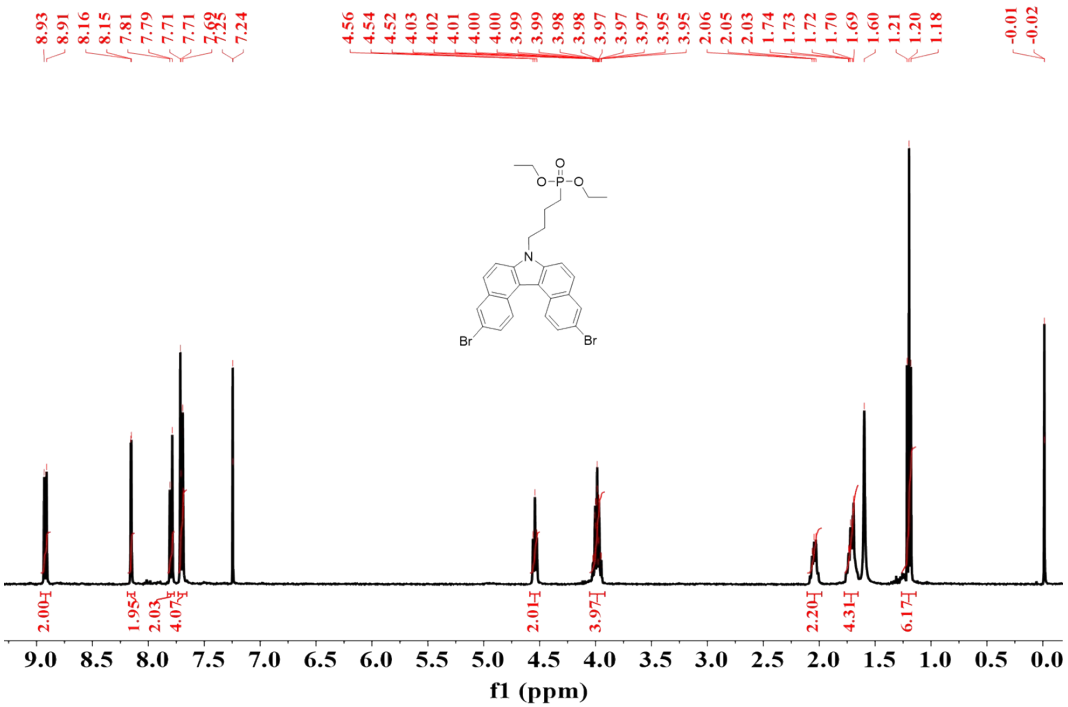

Figure S2. ^{1}H NMR spectrum for compund 3.

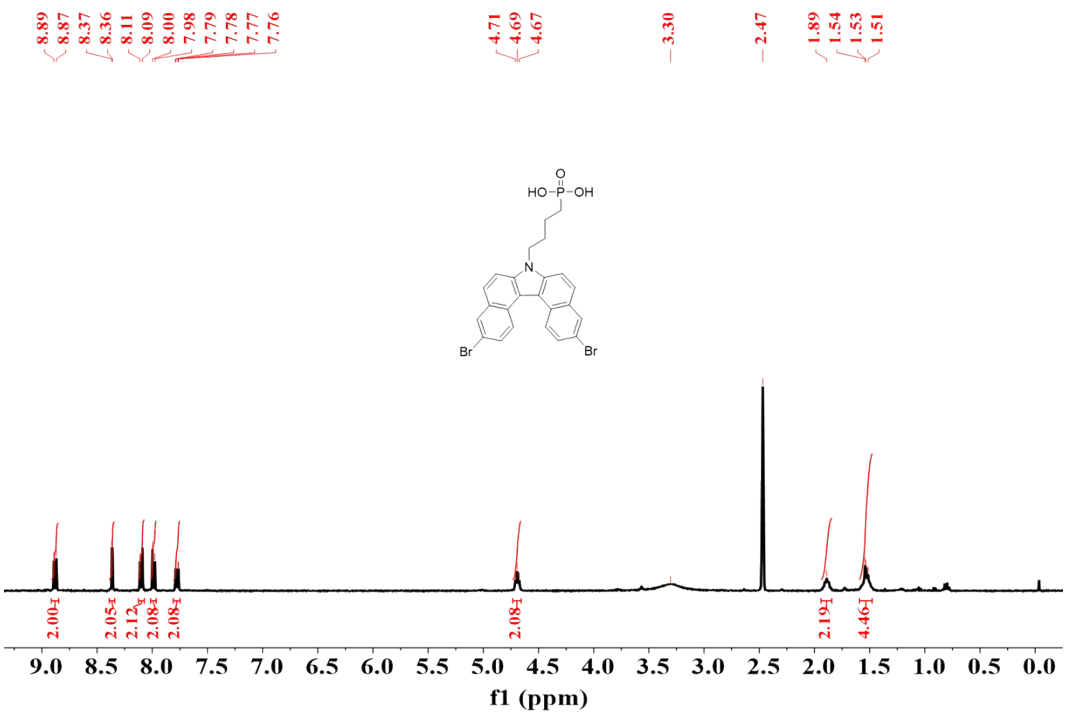

Figure S3. ^{1}H NMR spectrum for DCB-Br-2.

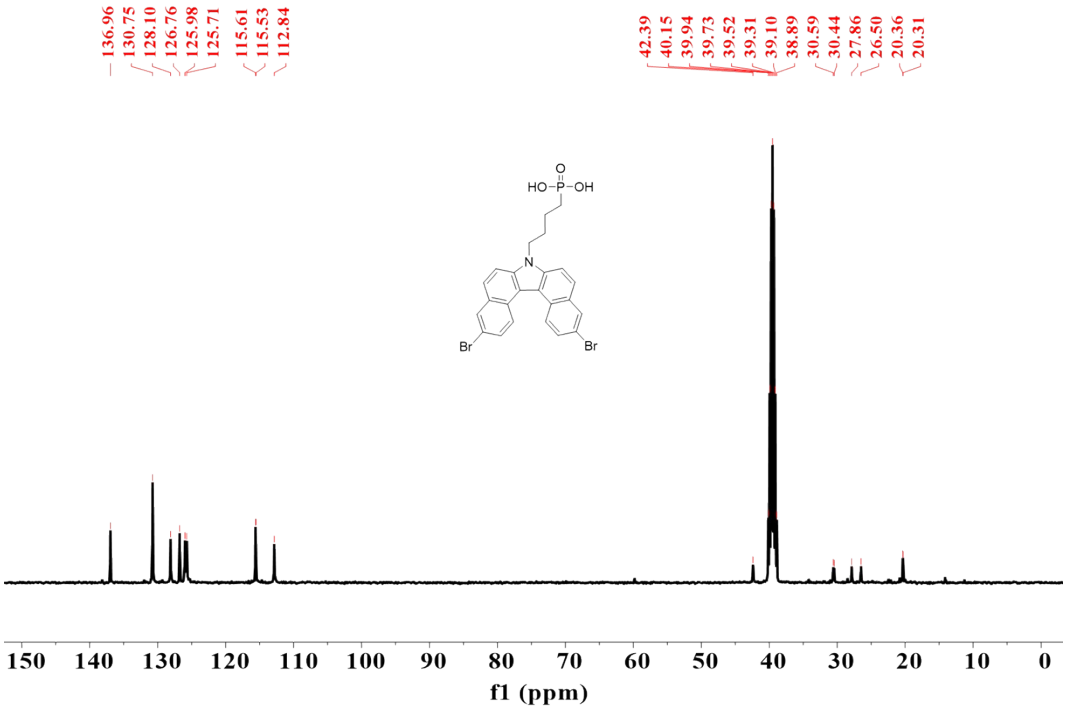

Figure S4. ^{13}C NMR spectrum for DCB-Br-2.

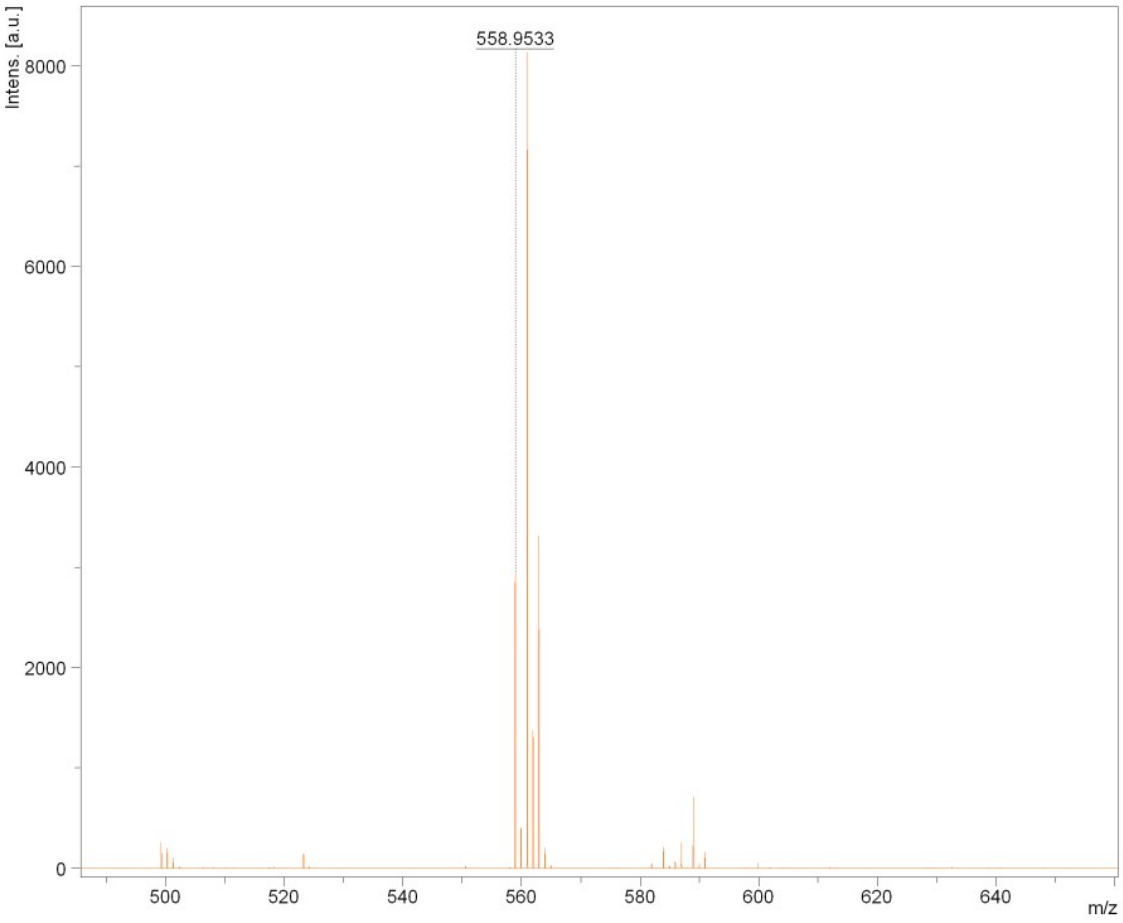

Figure S5. MADLI-TOF mass spectrometry for DCB-Br-2.

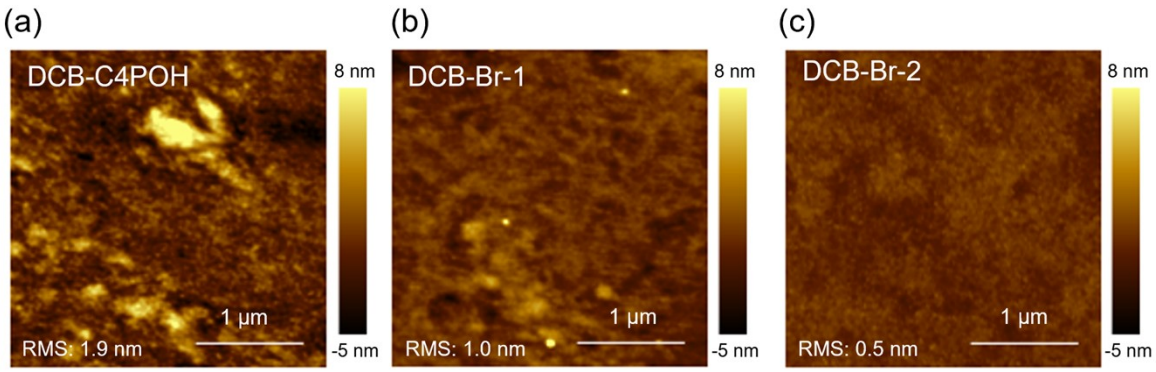

Figure S6. AFM images of different SAMs DCB-C4POH (a), DCB-Br-1 (b), and DCB-Br-2 (c) deposited on ITO substrates.

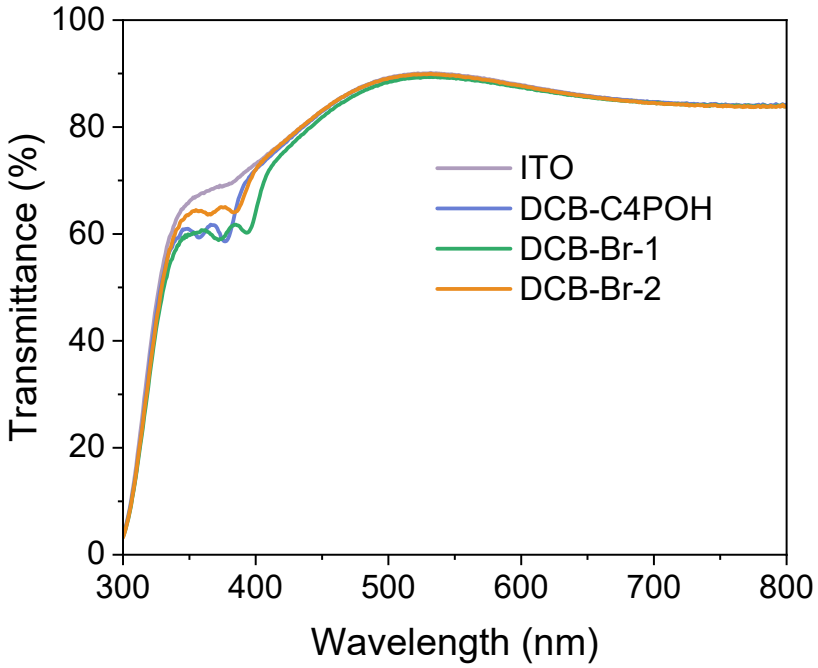

Figure S7. Transmittance spectra of bare ITO and ITO deposited with different SAMs.

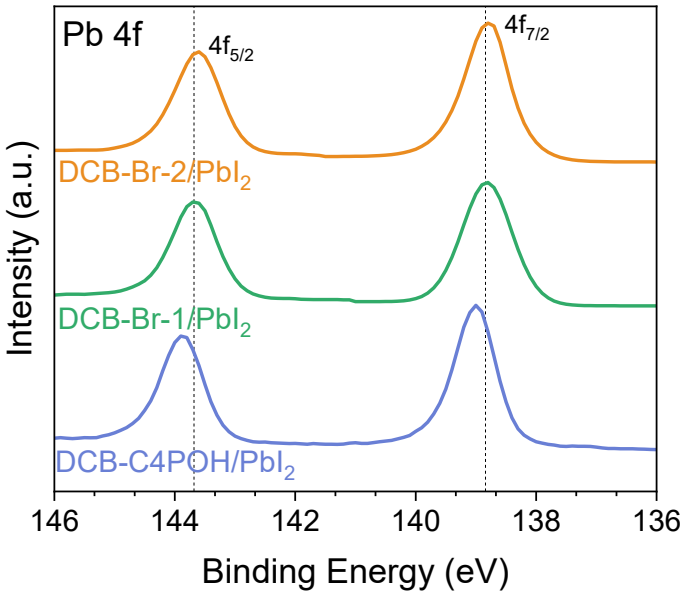

Figure S8. XPS spectra of Pb 4f of ITO/SAMs/PbI_2.

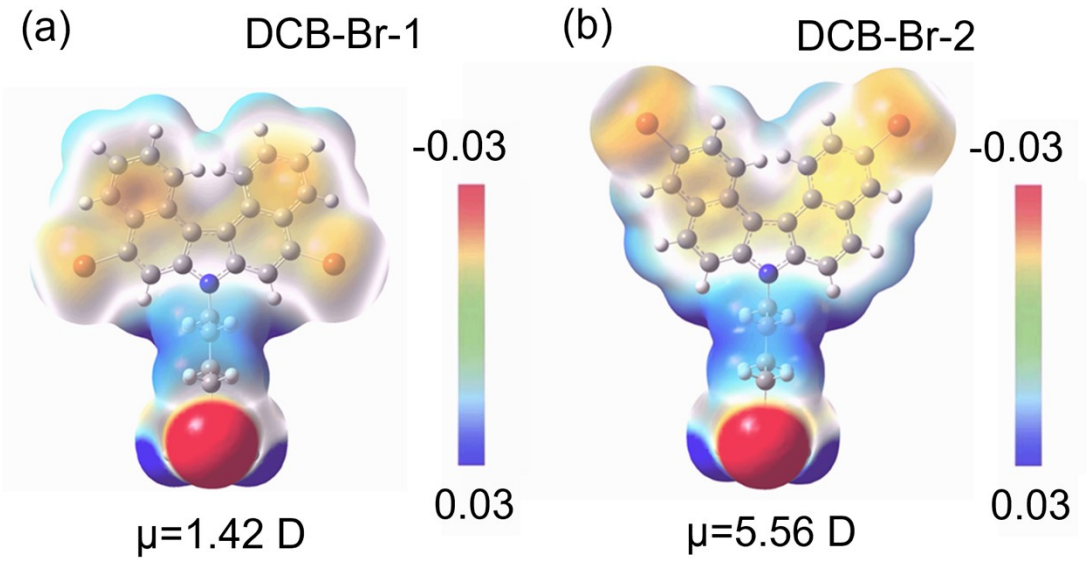

Figure S9. Calculated ESP of DCB-Br-1 (a), and DCB-Br-2 (b).

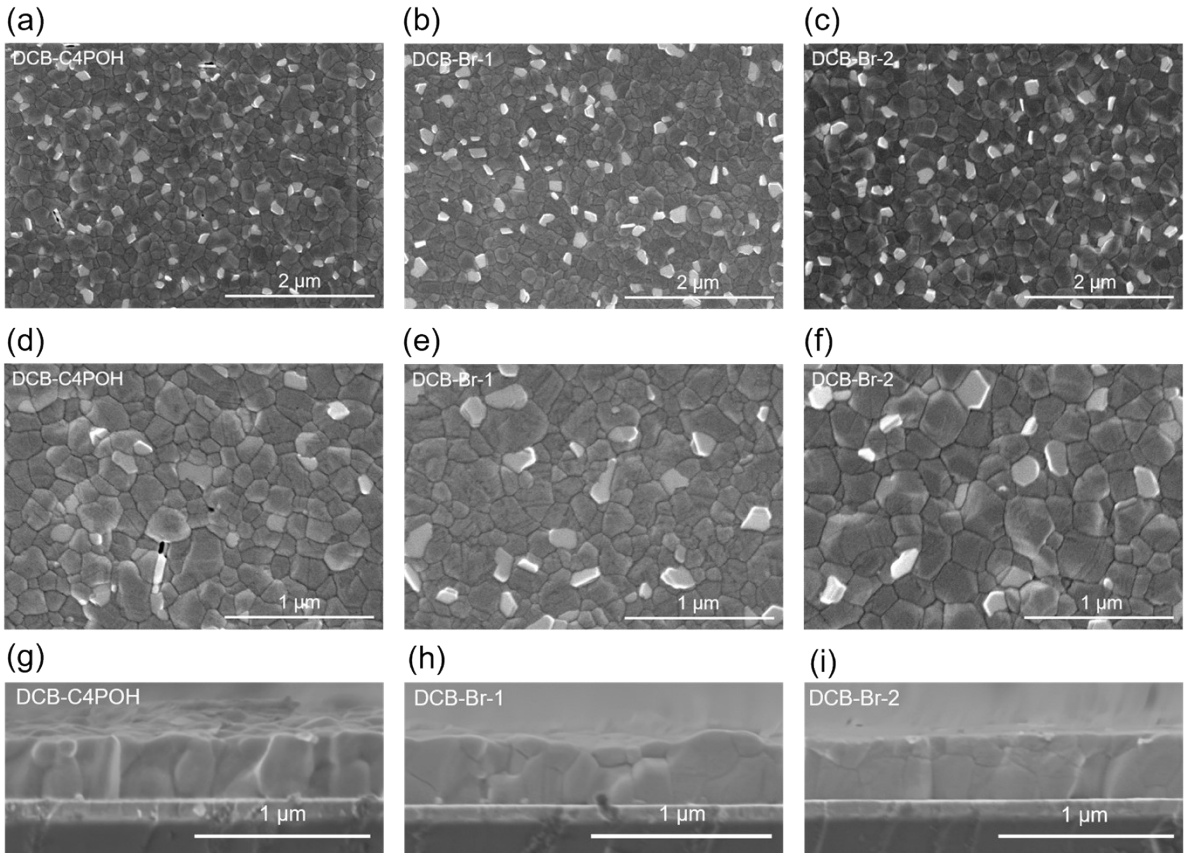

Figure S10. SEM images of perovskite films deposited on ITO/DCB-C4POH (a, d, g), ITO/DCB-Br-1 (b, e, h), and ITO/DCB-Br-2 (c, f, i) substrates.

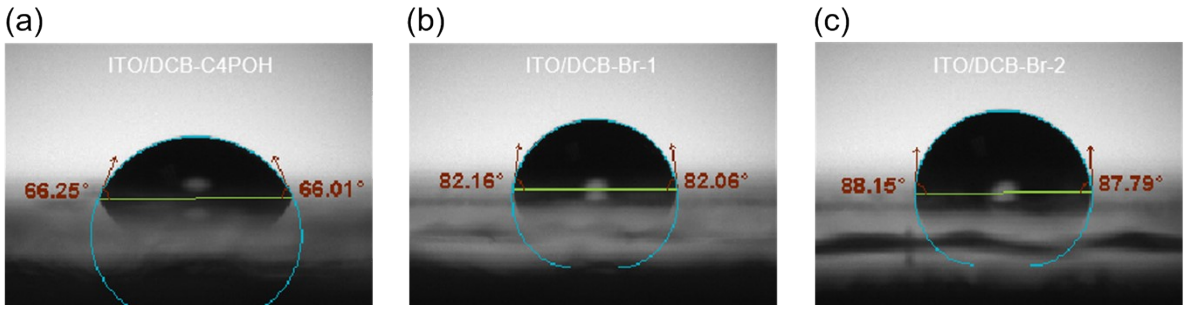

Figure S11. Contact angle measurements using DI water as a test solvent. Contact angle of ITO/DCB-C4POH (a), ITO/DCB-Br-1 (b), and ITO/DCB-Br-2 (c).

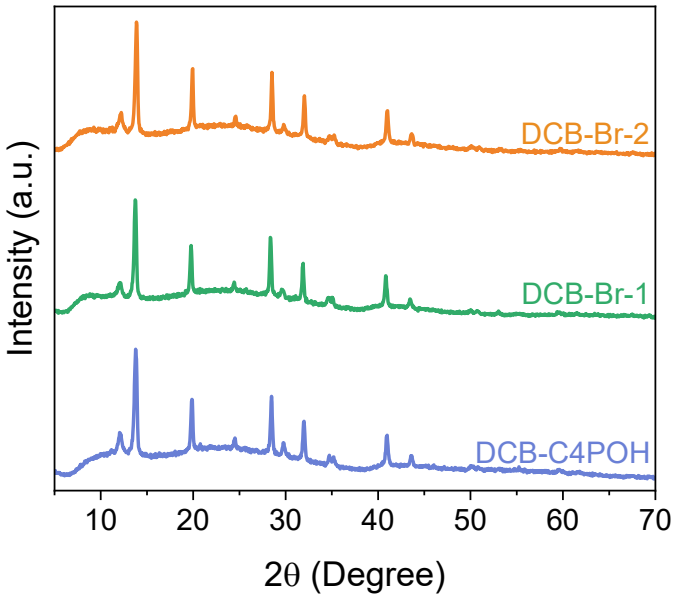

Figure S12. XRD patterns of WBG PVSK deposited on ITO/DCB-C4POH, ITO/DCB-Br-1, and ITO/DCB-Br-2 substrates.

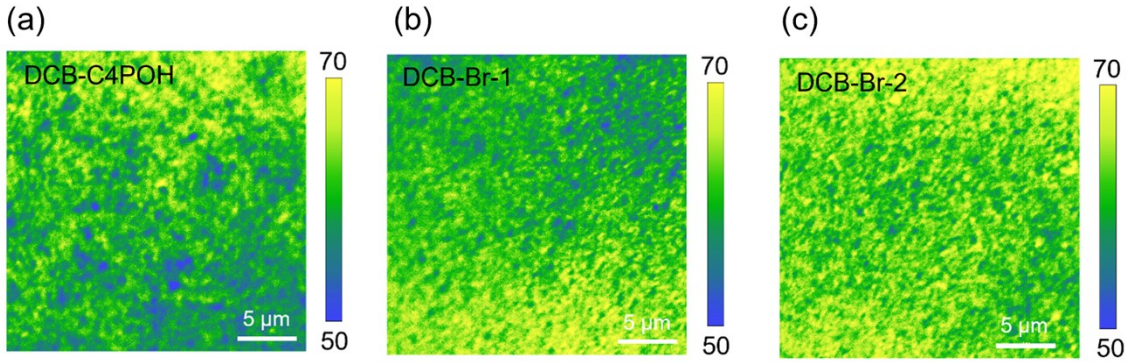

Figure S13. Confocal PL mapping of perovskite films deposited on ITO/DCB-C4POH (a), ITO/DCB-Br-1(b), and ITO/DCB-Br-2 substrates (c).

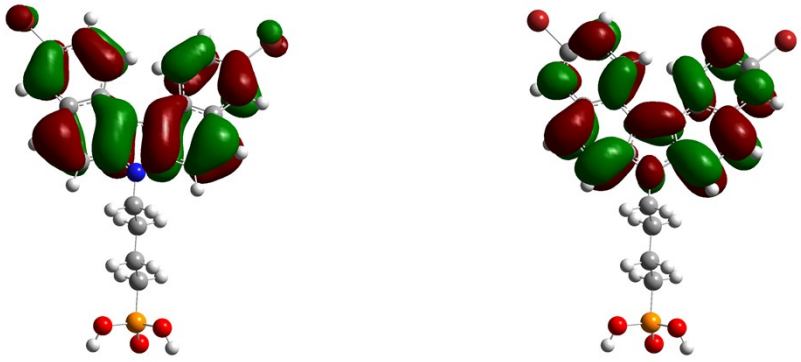

Figure S14. Calculated HOMO and LUMO of DCB-Br-2.

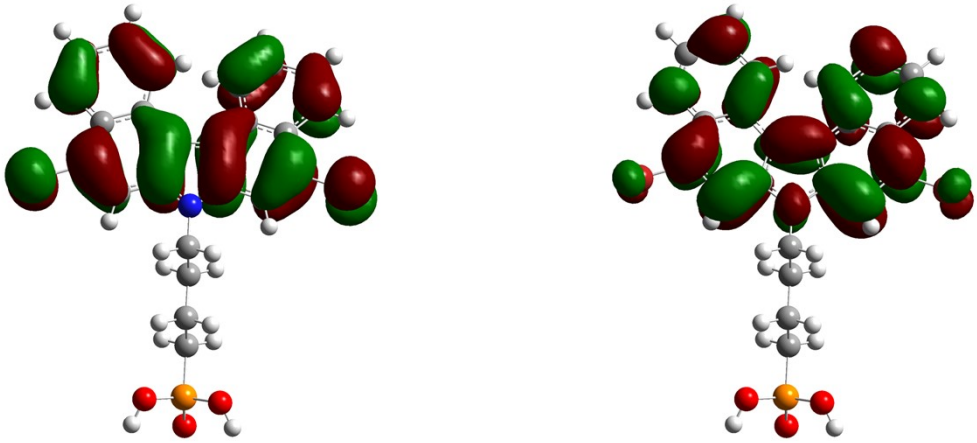

Figure S15. Calculated HOMO and LUMO of DCB-Br-1.

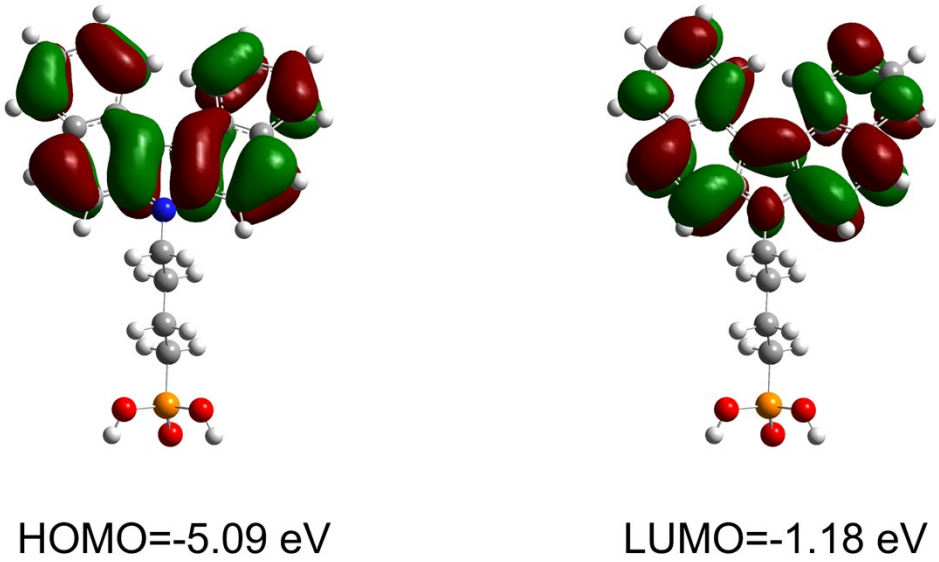

Figure S16. Calculated HOMO and LUMO of DCB-C4POH.

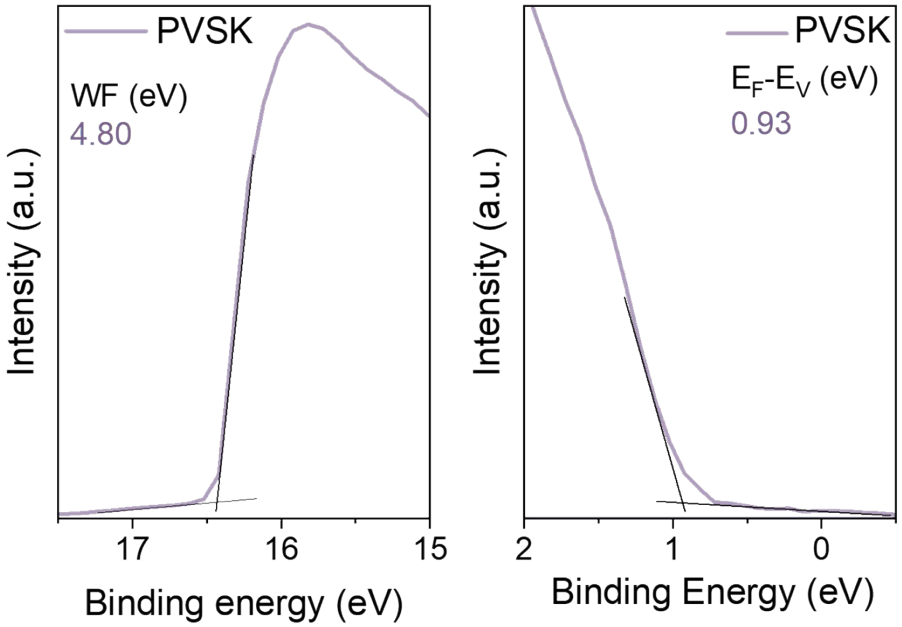

Figure S17. UPS spectra of the perovskite.

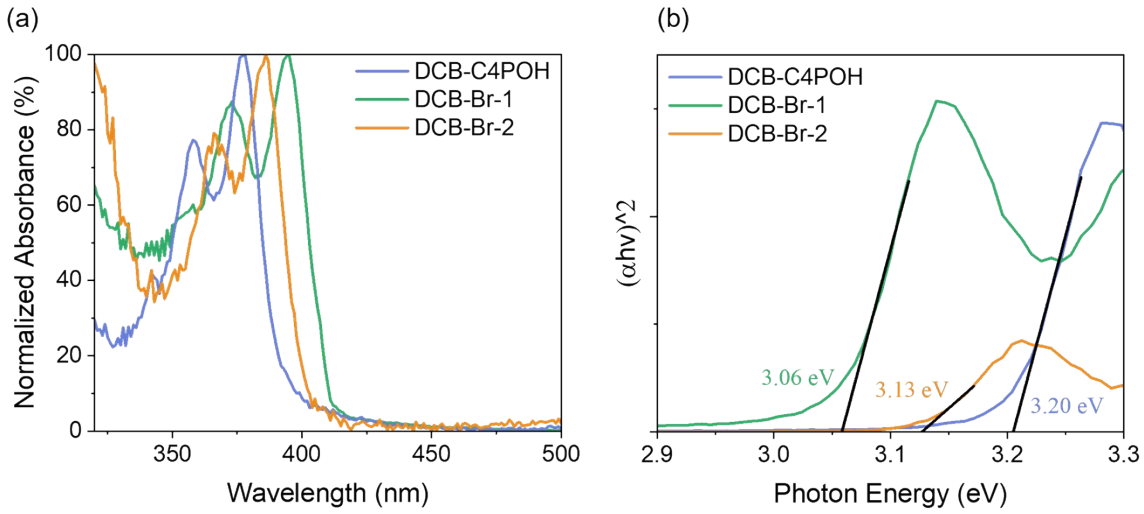

Figure S18. Normalized absorbance spectra (a) and tauc plots (b) of DCB-C4POH, DCB-Br-1, and DCB-Br-2.

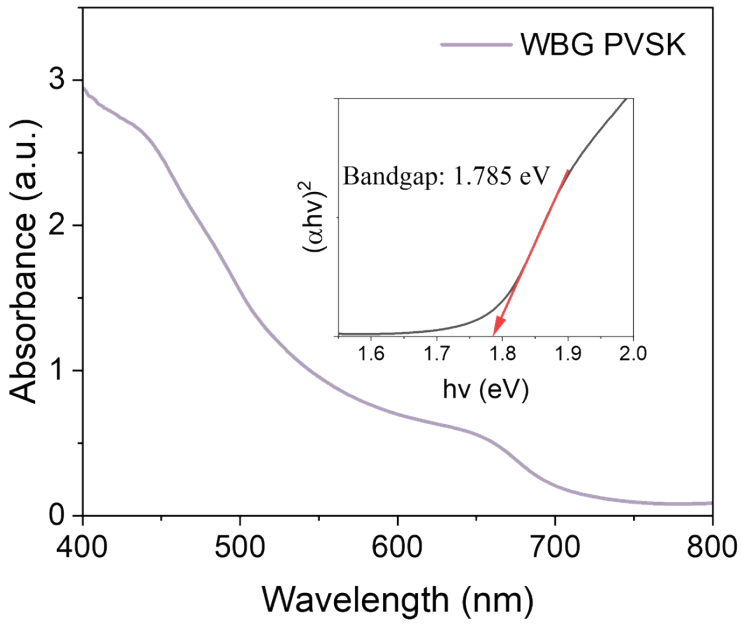

Figure S19. Absorbance spectrum and tauc plot (inset) of the WBG PVSK.

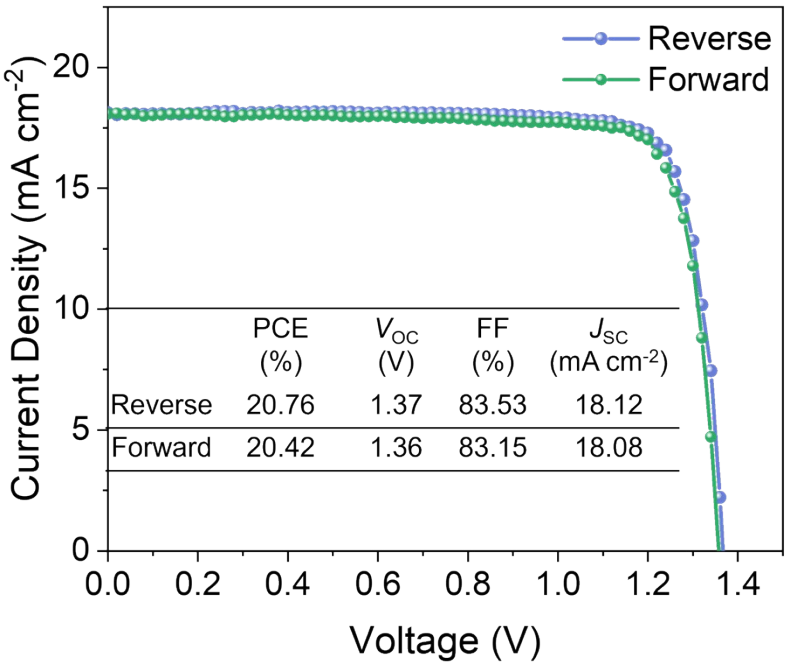

Figure S20. Reverse and forward scans of a champion DCB-Br-2-based WBG PSCs.

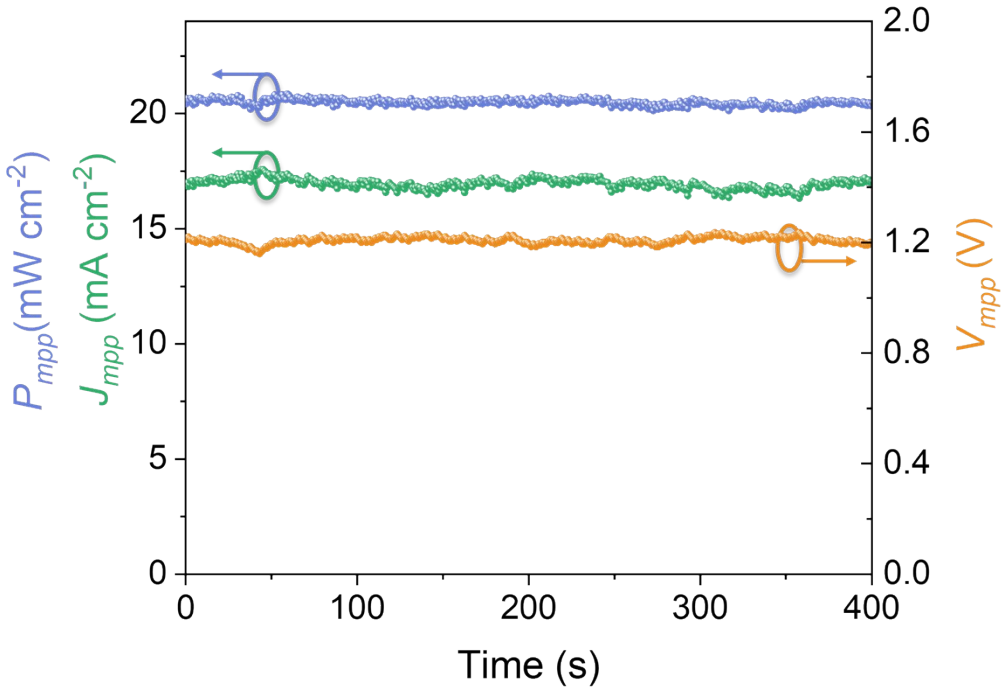

Figure S21. 400 seconds of MPP tracking of the DCB-Br-2-based WBG single-junction PSC. Blue: maximum power output (P_{mpp}); green: current density at the maximum power point (J_{mpp}); orange: voltage at the maximum power point (V_{mpp}).

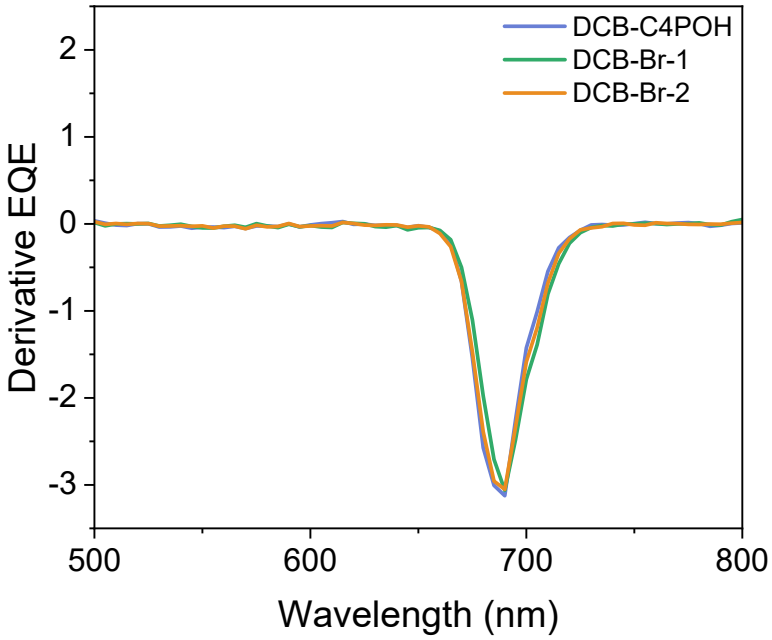

Figure S22. First derivative of EQE spectra with different HTLs to determine the bandgap.

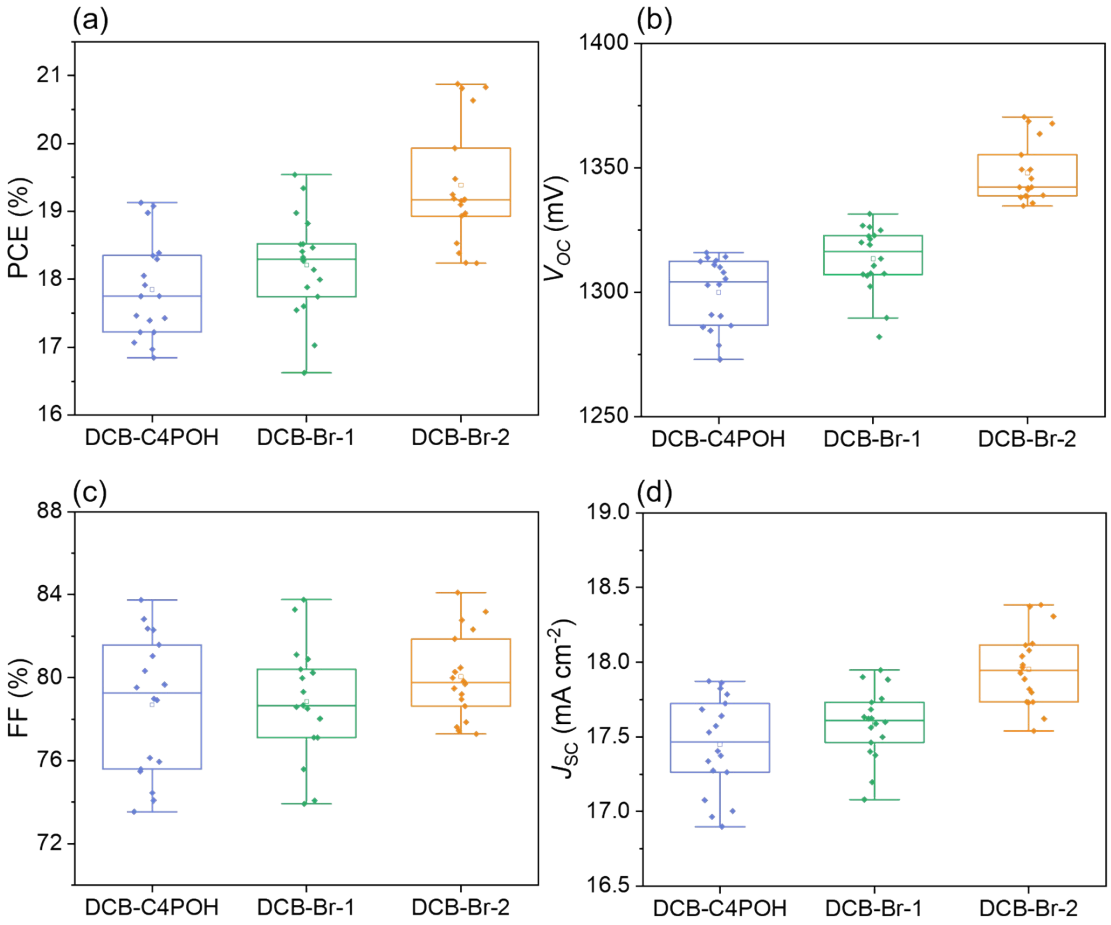

Figure S23. Statistic PCE (a), V_{OC} (b), FF (c), and J_{SC} (d) distribution of WBG PSCs with different HTLs (18 devices for each type).

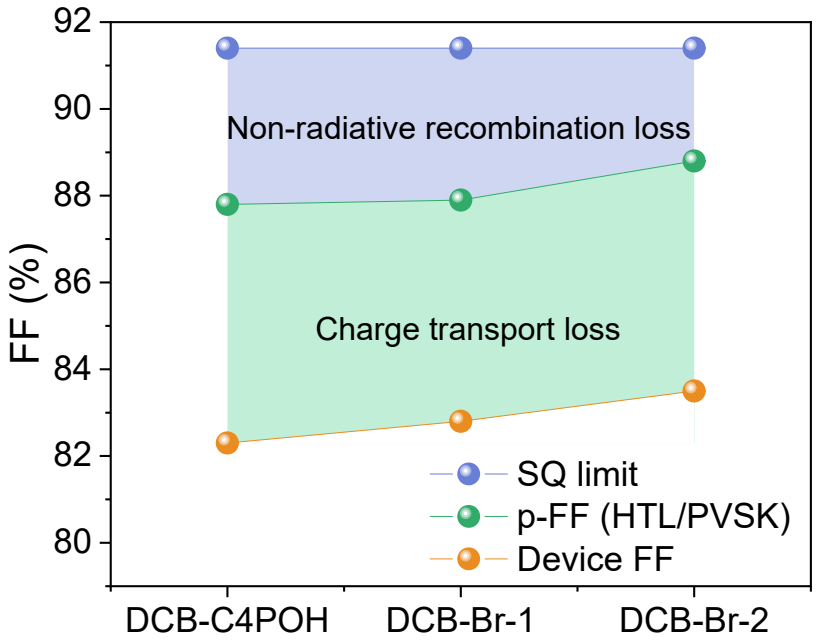

Figure S24. Schematic of FF loss mechanisms. The SQ limit is obtained from the radiative recombination limit which is 91.5% for 1.79 eV perovskites.[5]

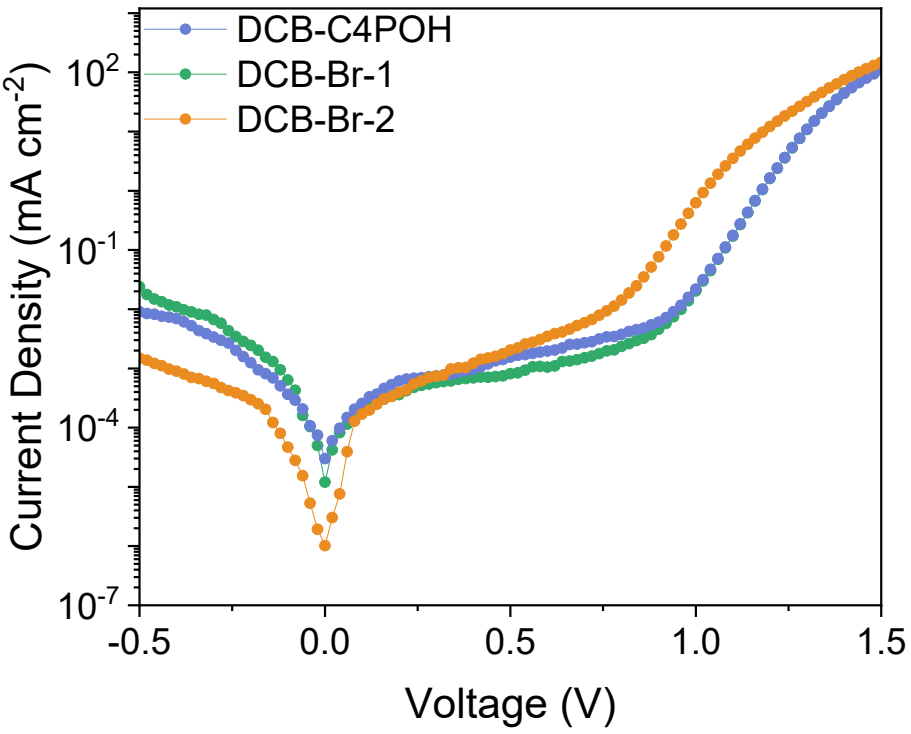

Figure S25. Dark current density-voltage of WBG PSCs.

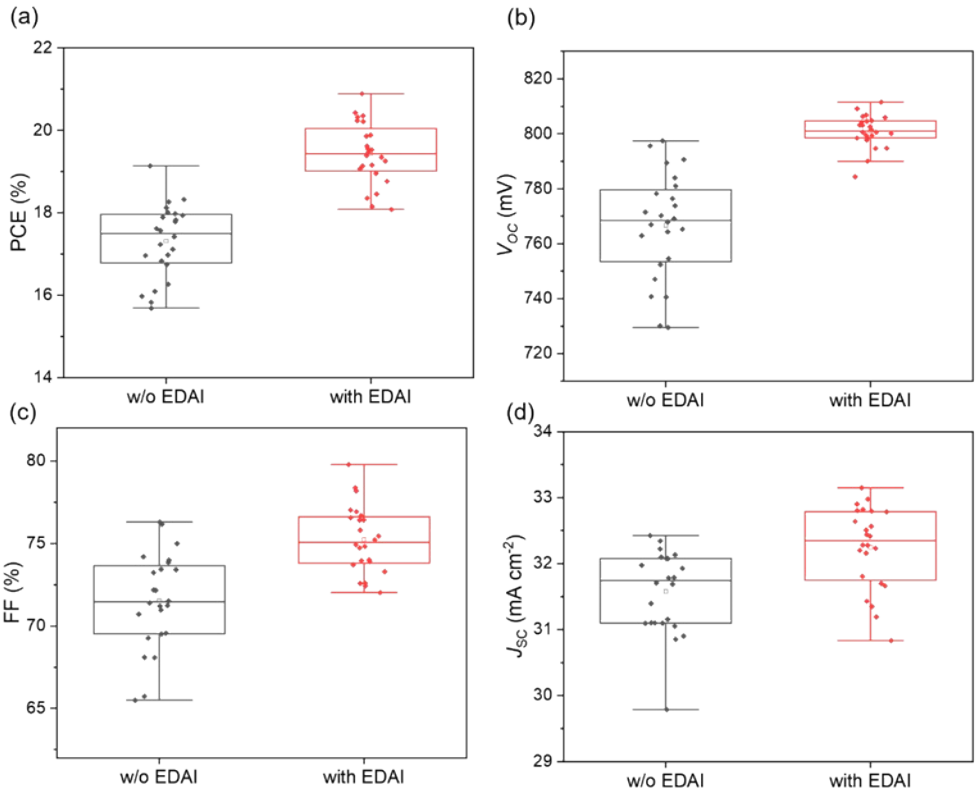

Figure S26. Statistic PCE (a), V_{OC} (b), FF (c), and J_{SC} (d) distribution of NBG PSCs with and without EDAI post treatment (24 devices in count).

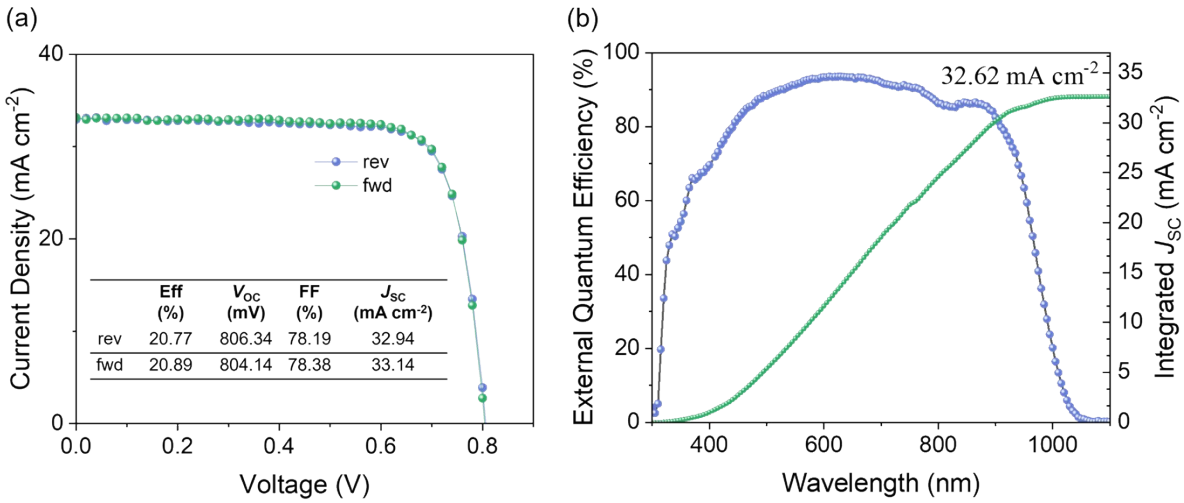

Figure S27. (a) JV curves and the photovoltaic parameters of the NBG PSC. (b) EQE spectrum and the integrated J_{SC} of the NBG PSC.

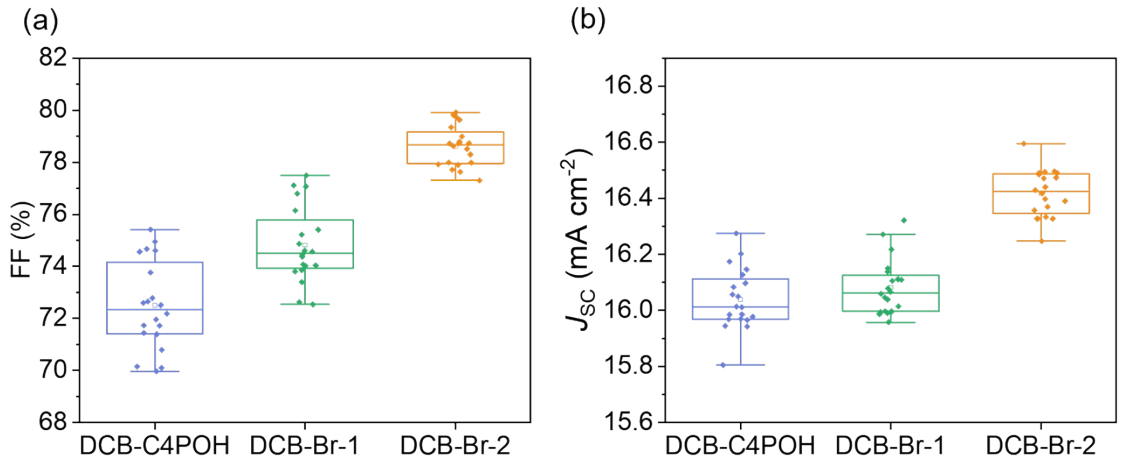

Figure S28. Statistic FF (a), and J_{SC} (b) distribution of all-perovskite TSCs based on different HTLs in WBG subcells.

Table S1. Carrier lifetimes of PVSKs deposited on various SAM HTLs derived from the fitting of TRPL measurements.

	y_0	A1	τ1 (ns)	A2	τ2 (ns)
DCB-C4POH	0.033	89.50	40.02	0.16	776.19
DCB-Br-1	0.026	33.14	33.36	0.24	783.46
DCB-Br-2	0.025	171.27	28.54	0.21	1489.18

Table S2. Photovoltaic performance of the literature reported WBG (1.76 ~ 1.80 eV) PSCs.

Bandgap (eV)	V_{OC} (V)	J_{SC} (mA cm^{-2})	FF (%)	PCE (%)	References
1.76	1.22	17.40	81.60	17.30	[6]
1.77	1.29	15.00	77.90	15.10	[7]
1.77	1.28	17.20	80.29	17.72	[8]
1.77	1.24	17.50	81.40	17.60	[9]
1.77	1.31	18.47	78.00	18.90	[10]
1.77	1.31	79.18	17.85	18.46	[2]
1.77	1.23	18.10	82.80	18.50	[11]
1.77	1.27	17.70	84.50	19.10	[12]
1.77	1.31	17.93	82.31	19.33	[13]
1.77	1.32	18.22	84.08	19.85	[14]
1.77	1.33	16.43	80.94	17.72	[15]
1.77	1.339	16.65	84.65	18.88	[3]
1.78	1.23	16.50	78.90	16.00	[16]
1.78	1.324	17.90	83.00	19.60	[17]
1.78	1.36	/	/	/	[18]
1.78	1.31	17.20	83.00	18.70	[19]
1.79	1.33	17.29	83.90	19.30	[20]
1.79	1.34	17.80	83.10	19.53	[21]
1.79	1.32	18.01	84.37	20.06	[22]
1.79	1.26	17.90	78.90	17.80	[23]
1.79	1.25	16.90	80.70	16.90	[24]
1.80	1.26	17.40	79.70	17.70	[25]
1.80	1.34	17.90	83.60	20.10	[26]
1.80	1.27	16.20	82.30	16.94	[27]
1.80	1.26	18.07	83.44	18.92	[28]
1.80	1.36	18.11	81.50	20.00	[29]

Table S3. Pseudo-*JV* parameters of the PVSKs with different HTLs as obtained from intensity dependent PLQY measurements. Assuming a J_{SC} of 18.5 mA cm^{-2}.

	p-V_{OC} (V)	p-FF (%)	p-J_{SC} (mA cm^{-2})	p-PCE (%)
DCB-C4POH	1.369	87.8	18.5	22.24
DCB-Br-1	1.379	87.9	18.5	22.42
DCB-Br-2	1.397	88.8	18.5	22.95

Table S4. *JV* parameters of all-perovskite TSCs based on different SAM HTLs. The aperture area is 0.055 cm^2.

	Scan direction	PCE (%)	V_{OC} (V)	FF (%)	J_{SC} (mA cm^{-2})
DCB-C4POH	Reverse	24.67	2.03	75.41	16.12
	Forward	24.12	2.02	74.75	15.98
DCB-Br-1	Reverse	25.88	2.07	77.50	16.13
	Forward	25.36	2.05	76.88	16.05
DCB-Br-2	Reverse	27.70	2.11	79.81	16.49
	Forward	27.14	2.10	78.79	16.44

References

1. A. Al-Ashouri, E. Köhnen, B. Li, A. Magomedov, H. Hempel, P. Caprioglio, J. A. Márquez, A. B. Morales Vilches, E. Kasparavicius, J. A. Smith, N. Phung, D. Menzel, M. Grischek, L. Kegelmann, D. Skroblin, C. Gollwitzer, T. Malinauskas, M. Jošt, G. Matič, B. Rech, R. Schlatmann, M. Topič, L. Korte, A. Abate, B. Stannowski, D. Neher, M. Stolterfoht, T. Unold, V. Getautis and S. Albrecht, *Science*, 2020, **370**, 1300-1309.
2. R. He, W. Wang, Z. Yi, F. Lang, C. Chen, J. Luo, J. Zhu, J. Thiesbrummel, S. Shah, K. Wei, Y. Luo, C. Wang, H. Lai, H. Huang, J. Zhou, B. Zou, X. Yin, S. Ren, X. Hao, L. Wu, J. Zhang, J. Zhang, M. Stolterfoht, F. Fu, W. Tang and D. Zhao, *Nature*, 2023, **618**, 80-86.
3. Z. Yi, W. Wang, R. He, J. Zhu, W. Jiao, Y. Luo, Y. Xu, Y. Wang, Z. Zeng, K. Wei, J. Zhang, S.-W. Tsang, C. Chen, W. Tang and D. Zhao, *Energy & Environmental Science*, 2024, **17**, 202-209.
4. C. Maeda, T. Todaka and T. Ema, *Organic Letters*, 2015, **17**, 3090-3093.
5. S. Rühle, *Solar Energy*, 2016, **130**, 139-147.
6. R. Lin, J. Xu, M. Wei, Y. Wang, Z. Qin, Z. Liu, J. Wu, K. Xiao, B. Chen, S. M. Park, G. Chen, H. R. Atapattu, K. R. Graham, J. Xu, J. Zhu, L. Li, C. Zhang, E. H. Sargent and H. Tan, *Nature*, 2022, **603**, 73-78.
7. H. Lai, J. Luo, Y. Zwirner, S. Olthof, A. Wieczorek, F. Ye, Q. Jeangros, X. Yin, F. Akhundova, T. Ma, R. He, R. K. Kothandaraman, X. Chin, E. Gilshtein, A. Müller, C. Wang, J. Thiesbrummel, S. Siol, J. M. Prieto, T. Unold, M. Stolterfoht, C. Chen, A. N. Tiwari, D. Zhao and F. Fu, *Advanced Energy Materials*, 2022, **12**, 2202438.
8. R. He, Z. Yi, Y. Luo, J. Luo, Q. Wei, H. Lai, H. Huang, B. Zou, G. Cui, W. Wang, C. Xiao, S. Ren, C. Chen, C. Wang, G. Xing, F. Fu and D. Zhao, *Advanced Science*, 2022, **9**, 2203210.
9. P. Wu, J. Wen, Y. Wang, Z. Liu, R. Lin, H. Li, H. Luo and H. Tan, *Advanced Energy Materials*, 2022, **12**, 2202948.
10. X. Zhou, H. Lai, T. Huang, C. Chen, Z. Xu, Y. Yang, S. Wu, X. Xiao, L. Chen, C. J. Brabec, Y. Mai and F. Guo, *ACS Energy Letters*, 2023, **8**, 502-512.
11. T. Li, J. Xu, R. Lin, S. Teale, H. Li, Z. Liu, C. Duan, Q. Zhao, K. Xiao, P. Wu, B. Chen, S. Jiang, S. Xiong, H. Luo, S. Wan, L. Li, Q. Bao, Y. Tian, X. Gao, J. Xie, E. H. Sargent and H. Tan, *Nature Energy*, 2023, **8**, 610-620.
12. Y. Wang, R. Lin, X. Wang, C. Liu, Y. Ahmed, Z. Huang, Z. Zhang, H. Li, M. Zhang, Y. Gao, H. Luo, P. Wu, H. Gao, X. Zheng, M. Li, Z. Liu, W. Kong, L. Li, K. Liu, M. I. Saidaminov, L. Zhang and H. Tan, *Nature Communications*, 2023, **14**, 1819.
13. J. Zhu, Y. Luo, R. He, C. Chen, Y. Wang, J. Luo, Z. Yi, J. Thiesbrummel, C. Wang, F. Lang, H. Lai, Y. Xu, J. Wang, Z. Zhang, W. Liang, G. Cui, S. Ren, X. Hao, H. Huang, Y. Wang, F. Yao, Q. Lin, L. Wu, J. Zhang, M. Stolterfoht, F. Fu and D. Zhao, *Nature Energy*, 2023, **8**, 714-724.
14. H. Liu, J. Dong, P. Wang, B. Shi, Y. Zhao and X. Zhang, *Advanced Functional Materials*, 2023, **33**, 2303673.
15. G. Xie, H. Li, X. Wang, J. Fang, D. Lin, D. Wang, S. Li, S. He and L. Qiu, *Advanced Functional Materials*, 2023, **33**, 2308794.
16. Z. Yu, Z. Yang, Z. Ni, Y. Shao, B. Chen, Y. Lin, H. Wei, Z. J. Yu, Z. Holman and J. Huang, *Nature Energy*, 2020, **5**, 657-665.
17. J. Wen, Y. Zhao, P. Wu, Y. Liu, X. Zheng, R. Lin, S. Wan, K. Li, H. Luo, Y. Tian, L. Li and H. Tan, *Nature Communications*, 2023, **14**, 7118.
18. H. Cui, L. Huang, S. Zhou, C. Wang, X. Hu, H. Guan, S. Wang, W. Shao, D. Pu, K. Dong, J. Zhou, P. Jia, W. Wang, C. Tao, W. Ke and G. Fang, *Energy & Environmental Science*, 2023, **16**, 5992-6002.
19. S. Li, Z. Zheng, J. Ju, S. Cheng, F. Chen, Z. Xue, L. Ma and Z. Wang, *Advanced Materials*, 2024, **36**, e2307701.

20. H. Chen, A. Maxwell, C. Li, S. Teale, B. Chen, T. Zhu, E. Ugur, G. Harrison, L. Grater, J. Wang, Z. Wang, L. Zeng, S. M. Park, L. Chen, P. Serles, R. A. Awni, B. Subedi, X. Zheng, C. Xiao, N. J. Podraza, T. Filleter, C. Liu, Y. Yang, J. M. Luther, S. De Wolf, M. G. Kanatzidis, Y. Yan and E. H. Sargent, *Nature*, 2023, **613**, 676-681.
21. Y. An, N. Zhang, Z. Zeng, Y. Cai, W. Jiang, F. Qi, L. Ke, F. R. Lin, S. W. Tsang, T. Shi, A. K. Jen and H. L. Yip, *Advanced Materials*, 2024, **36**, e2306568.
22. L. Qiao, T. Ye, P. Wang, T. Wang, L. Zhang, R. Sun, W. Kong and X. Yang, *Advanced Functional Materials*, 2023, **34**, 2308908.
23. W. Chen, Y. Zhu, J. Xiu, G. Chen, H. Liang, S. Liu, H. Xue, E. Birgersson, J. W. Ho, X. Qin, J. Lin, R. Ma, T. Liu, Y. He, A. M.-C. Ng, X. Guo, Z. He, H. Yan, A. B. Djurišić and Y. Hou, *Nature Energy*, 2022, **7**, 229-237.
24. S. Qin, C. Lu, Z. Jia, Y. Wang, S. Li, W. Lai, P. Shi, R. Wang, C. Zhu, J. Du, J. Zhang, L. Meng and Y. Li, *Advanced Materials*, 2022, **34**, 2108829.
25. J. Wen, Y. Zhao, Z. Liu, H. Gao, R. Lin, S. Wan, C. Ji, K. Xiao, Y. Gao, Y. Tian, J. Xie, C. J. Brabec and H. Tan, *Advanced Materials*, 2022, **34**, 2110356.
26. Z. Li, X. Sun, X. Zheng, B. Li, D. Gao, S. Zhang, X. Wu, S. Li, J. Gong, J. M. Luther, Z. a. Li and Z. Zhu, *Science*, 2023, **382**, 284-289.
27. P. Caprioglio, J. A. Smith, R. D. J. Oliver, A. Dasgupta, S. Choudhary, M. D. Farrar, A. J. Ramadan, Y.-H. Lin, M. G. Christoforo, J. M. Ball, J. Diekmann, J. Thiesbrummel, K.-A. Zaininger, X. Shen, M. B. Johnston, D. Neher, M. Stolterfoht and H. J. Snaith, *Nature Communications*, 2023, **14**, 932.
28. Y. Tang, Y. Zhang, X. Zhou, T. Huang, K. Shen, K. Zhang, X. Du, T. Shi, X. Xiao, N. Li, C. J. Brabec, Y. Mai and F. Guo, *Nano Energy*, 2023, **114**, 108653.
29. F. Yang, P. Tockhorn, A. Musiienko, F. Lang, D. Menzel, R. Macqueen, E. Kohnen, K. Xu, S. Mariotti, D. Mantione, L. Merten, A. Hinderhofer, B. Li, D. R. Wargulski, S. P. Harvey, J. Zhang, F. Scheler, S. Berwig, M. Ross, J. Thiesbrummel, A. Al-Ashouri, K. O. Brinkmann, T. Riedl, F. Schreiber, D. Abou-Ras, H. Snaith, D. Neher, L. Korte, M. Stolterfoht and S. Albrecht, *Advanced Materials*, 2024, **36**, 2307743.